JOURNAL OF THERMOPHYSICS AND HEAT TRANSFER
Vol. 11, No. 3, July–September 1997

Infrared Imaging and Shock Visualization of Flow over Concave Blunt Bodies

K. B. Yüceil* and D. S. Dolling†
University of Texas at Austin, Austin, Texas 78712

Experiments have been made to determine if the unsteady flow induced by a streamwise cavity in the nose of a blunt body can reduce mean surface heat transfer rates compared to the same body without a cavity. Measurements were made at Mach 5 and included surface temperatures obtained using an infrared camera, fluctuating pressures at the cavity base, and bow shock visualization using planar laser Mie scattering. Cavities with a length-to-depth ratio of about 2 appear very promising in terms of reduced heating. Cavities for which the length-to-depth ratio varies from about 0.4 to 0.7 exhibit unstable, nonaxisymmetric surface temperature and cavity pressure histories. Instantaneous shock visualization reveals nonaxisymmetric shocks that correlate with the unstable pressure histories. Cavity resonance frequency decreases as the cavity depth increases and pressure fluctuations increase in amplitude. In all cases, the primary oscillation frequency agrees well with simple organ pipe theory.

Nomenclature

a = speed of sound
C_h = Stanton number, $q/\rho_\infty u_\infty c_p(T_{aw} - T_w)$
c_p = specific heat at constant pressure
D = cavity diameter
D_n = nose diameter
f = frequency
$G(f)$ = power spectral density
L = cavity depth
L' = distance between shock wave and cavity base
M = Mach number
P = base pressure
P_{t2} = total pressure behind the normal shock
$P1$ = temperature measurement point in the nose stagnation region
$P2$ = temperature measurement point at about 33 deg from the nose-tip
q = heat flux
R = specific gas constant
R_n = nose radius
T = temperature
T_{aw} = adiabatic wall temperature
T_w = measured nose surface temperature
u = flow velocity
γ = ratio of specific heats
Δy = offset in P/P_{t2}
δ = shock standoff distance
θ = angle measured from the nose stagnation point
λ = wavelength of pressure waves
ρ = fluid density
σ = standard deviation of fluctuating pressures

Subscripts
aw = adiabatic wall
b = baseline
n = nose
i = initial
p = primary resonance
$t2$ = conditions behind the normal shock
w = surface
0 = stagnation
∞ = freestream

Received Aug. 20, 1996; revision received Jan. 6, 1997; accepted for publication Jan. 8, 1997.

*Graduate Research Assistant, Center for Aeromechanics Research, Department of Aerospace Engineering and Engineering Mechanics; currently Assistant Professor, Department of Space Sciences and Technology, Istanbul Technical University, Istanbul, Turkey. Student Member AIAA.

†Professor, Center for Aeromechanics Research, Department of Aerospace Engineering and Engineering Mechanics. Associate Fellow AIAA.

Introduction

THERE is substantial interest within the U.S. Army in increasing the firing speeds of kinetic energy projectiles to improve their penetration characteristics.[1,2] Currently, speeds of 1.5–2 km/s at sea level can be attained without ablation of the projectile tip by using materials such as tungsten. However, even with tungsten, the extremely high heating rates above 2 km/s can cause tip ablation, which can result in undesirable aerodynamics and unreliable penetration characteristics. There is consequently a need to develop innovative active or passive techniques to reduce nose-tip heating rates. For reliability in the field, such techniques must be mechanically simple and inexpensive.

More than 30 years ago Stallings and Burbank[3] reported that the stagnation point heat transfer rate for an axisymmetric concave nose at supersonic Mach numbers could be 20% of that for a hemisphere–cylinder in steady flow. They also noted that both steady and unsteady flows could occur with such a configuration. The unsteady flow was sporadic and more predominant at small angle of attack and high Mach numbers. While such studies dealt more with fundamental aspects of the flow around a concave blunt nose, more recent ones[4–7] have focused on specific nose-cavity configurations designed to utilize this useful outcome of reduced heat transfer. Conical cavities with a circular base, which are typical of missile-seeker configurations with forward looking sensors, have received considerable attention. Huebner and Utreja[4] showed that the heat transfer coefficient distribution along the cavity walls at Mach 10 agreed well with the Mach 3.5 data of Stallings and Burbank,[3] even though the cavity geometries were different. The unsteady nature of the flow inside the cavity has also been investigated both experimentally[4,6] and numerically.[5] Sambamurthi et al.[5] obtained a good correlation between numerical results and experiments for the unsteady behavior of the shock. In the study of Marquart et al.[6] a laser interferometer was used to record the bow shock unsteadiness. They found that the shock motion lagged the fluctuating pressures in the cavity,

implying that the cavity pressure variations drove the bow shock oscillation. Huebner and Utreja[8] gave a detailed description of the bow-shock behavior for the same nose-cavity configuration at Mach 10. They found a stable oscillating bow shock in the majority of the tests, but they also documented and discussed a violent, unsteady bow shock motion that was observed during one of the tests.

Prior to the work reported in this paper some experimental results on the effects of a circular cavity in a hemispherical nose in a Mach 5 flow were obtained by the authors using a thermal imaging system.[9,10] The cavity base was spherical (to obtain a spherical nose when the cavity plug was pushed forward), and the effects of changes in cavity length L and diameter D were examined.[9] It was found that cavities with $L/D \leq 0.35$ had a stable cool ring. The cool ring is a region in the vicinity of the cavity lip in which temperatures are lower than those of a plain spherical nose and is a result of flow separation. Pressure oscillations inside the cavity had dominant frequencies that were close to organ pipe values that scaled with the cavity depth, as had been noted in earlier studies, i.e., Refs. 6 and 8. The effects of changes in cavity lip and base shape on the surface temperatures were also examined.[10,11] While changes in cavity lip or base shape had a large effect on the surface temperatures for some cavity depths, they had little effect on the fluctuating pressures for almost all cavity depths tested. The most important effect of lip shape on the temperature measurements was the elimination of the cool ring when the sharp lip was replaced by a rounded lip. A cool ring was also observed in a much deeper cavity case ($L/D = 1.2$) with some indication that much deeper cavities would provide even lower surface temperatures. It was also found that certain cavities had unstable and nonaxisymmetric temperature and fluctuating pressure histories. However, model constraints precluded the study of much deeper cavities ($L/D > 1.2$) and a detailed investigation of the unstable range. This lack of information led to the investigation reported in this paper.

Most recently, computations reported in Ref. 12 strongly imply that in the case of shallow cavities it is freestream noise that drives the resonant pressure oscillations. It appears that if the freestream noise has energy in a small bandwidth of frequencies around the primary mode then resonance will occur. In contrast it appears that for relatively deep cavities the flow is unstable and self-sustaining, i.e., will resonate without freestream noise. The latter observation is an encouraging one because it will be shown in this paper that it is in this depth regime that substantial heating reductions can be obtained.

In the study reported here, the fundamental goal is to determine whether stagnation region heat transfer can be reduced by using a simple streamwise, circular cavity in a hemispherical nose. The focus is on a configuration with a sharp lip and flat base for a wide range of cavity depths ($0.235 \leq L/D \leq 2.0$). An infrared camera was used for thermal imaging to obtain surface temperatures and heat transfer rates. In addition, planar laser Mie scattering (PLMS) has been used in conjunction with measurements of fluctuating base pressures to examine the relation between the instantaneous shape of the bow shock wave and the corresponding cavity base pressure.

In applications, the cavity will constitute a small part of the projectile body that usually has a conical nose section and a long cylindrical body. The nose-tip diameter is generally much smaller than the body diameter suggesting that the instabilities in the cavity will not affect significantly the overall aerodynamics of the projectile. However, further study is needed to accurately assess the effects of nose-cavity on aerodynamic characteristics and flight stability.

Experimental Program and Analysis Techniques

Wind Tunnel and Models

Experiments were conducted in the Mach 5 blowdown wind tunnel of the University of Texas at Austin. The test section is 17.78 cm high by 15.24 cm wide (7 by 6 in.) and has two circular observation windows. The tunnel was operated at a nominal stagnation pressure of 2.30 MPa (333 psia) and a nominal stagnation temperature of 370 K (666 °R). Because of the long testing times (≈30 s) required for the infrared (IR) camera and PLMS measurements, stagnation pressure and temperatures varied by about ±0.02 MPa and ±5 K from test to test. At the freestream Mach number of 4.95, these conditions generate a nominal freestream unit Reynolds number of 50×10^6 m^{-1} (1.52×10^7 ft^{-1}) and a freestream velocity of 758 m/s (2575 ft/s).

The model was a hemispherically blunted cylinder as shown in Fig. 1. Two models, one 5.08 cm (2 in.) in diameter and the other 3.05 cm (1.2 in.) in diameter with a variable-length cavity at the tip, were used. The cavity diameter was one-half of the model (nose) diameter in both cases. However, some additional fluctuating pressure measurements[9] were made with a cavity of one-fourth of the nose diameter, i.e., 1.27 cm, using the bigger model. The models were installed on the centerline of the test section at zero angle of attack using streamlined supports attached to the tunnel floor. The viewing window was made of zinc selenide (for maximum transmission of IR radiation) and was on loan from NASA Langley Research Center.

All of the experiments (except the baseline case) were conducted using a sharp lip and flat cavity base. For this case, an insert with a spherical end was used to obtain the plain spherical nose geometry (see Fig. 1). Most of the tests were conducted using the 5.08-cm diam (bigger) model. The smaller model (3.05 cm diam) was made of brass and had a single pressure transducer installed at the center of the flat cavity base. It was used to 1) check that the fluctuating pressure signals were not a function of the model size (there was initially some concern that during parts of the oscillation cycle tunnel sidewall interference might occur. Later tests proved this concern to be unfounded) and 2) to extend the results to higher values of L/D.

By changing the axial position of the cavity insert in the bigger model (see Fig. 1), values of (L/D) ranging from 0 to 2.25 for temperature measurements, and 0 to 1.5 for pressure measurements could be obtained. The pressure range was lower because of space constraints of installing pressure transducers. However, by using the smaller model, fluctuating pressures could be obtained for L/D up to 2.0. Table 1 gives the values of L/D used in the various tests. Note that L is the distance from the cavity lip to the cavity base-side wall junction (see Fig. 1).

In this paper cavities are referred to as shallow, medium depth, and very deep according to the different flow phenomena associated with each category. The L/D range of each category cannot be defined with precision because changes in flow behavior do not occur abruptly. Generally, the term shal-

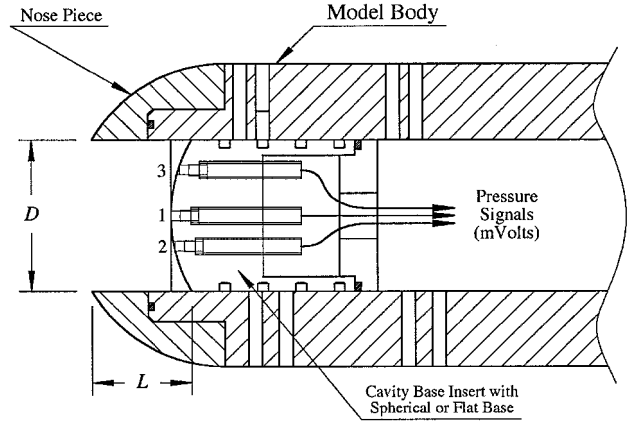

Fig. 1 Schematic view of model.

Table 1 Cavity sizes used in the experiments[a]

Category	Bigger model, IR	Bigger model, pressure	Smaller model, pressure
Shallow	0.235	0.23	0.30
Medium depth	0.40	0.59	0.35
	0.50	——	0.40
	0.60	——	0.50
	0.70	——	0.60
	——	——	0.70
Very deep	0.80	1.235	0.80
	0.90	——	1.00
	1.00	——	1.20
	1.50	——	1.50
	2.00	——	1.75
	——	——	2.00

[a]L/Ds for sharp lip/flat base configuration.

low is used if $(L/D) \leq 0.35$, medium depth if $0.40 \leq (L/D) \leq 0.70$, and very deep if $(L/D) \geq 0.75$. Exceptions are noted where appropriate.

Instrumentation and Data Acquisition

The IR camera system used in experiments is a commercial unit (Model 600) from Inframetrics, Inc. Thermal imaging has the advantage of being nonintrusive and a large volume of data can be acquired rapidly. To obtain accurate temperature measurements, the model material must have properties close to that of a blackbody. Also, since the IR scanner detects temperature differences between the target (i.e., model) and the background, the thermal gradient at the model surface should be maximized. Consequently, polycarbonate that has good structural properties and a very low thermal conductivity was selected as the material for the nose pieces. Independent temperature measurements made using the IR camera and thermocouples agreed to within 1–2 K.

Figure 1 also shows the inserts instrumented for fluctuating pressure measurements. Three Kulite pressure transducers (Model XCQ-062-50A) with frequency response of approximately 50 kHz and with a pressure range of 0–345 kPa (0–50 psia) were used. The transducers are nominally 1.63 mm (0.064 in.) in diameter and were installed with their axes parallel to the model axis and with their faces flush with the surface. The signals were amplified (by using either Dynamics (Model 7525), Measurements Group (Model 2311), or PARC (Model 113) amplifiers) and passed through Ithaco (Model 4213) Electronic Analog Filters with cutoff frequency set at 50 kHz. A LeCroy (Model 6810) Waveform Recorder with 12-bit resolution was used to digitize the signals. Data were acquired at 200 kHz/channel and a total of 524,288 points spanning a real time of 2.62144 s were taken per run. The data strings for each channel were broken into 512 records of 1024 data points each from which rms levels and power spectra were calculated. The frequency resolution for power spectra was 0.195 kHz. Stagnation temperature and pressure were recorded during the entire run.

Experimental Procedures

In the IR camera experiments, the model nose was initially shielded from the flow using an ordinary hollow racquetball cut in half that fitted snugly over the nose. Tests with a thermocouple at the nose showed a temperature rise of 2–3 K over 20–30 s, whereas without the cap the rise was 65–70 K. When steady-state stagnation conditions were well established, about 20 s after startup, the cap was removed by pulling the string attached to it. The IR video camera was operated continuously during the entire run. By matching the clocks on the camera and on the data acquisition system, the time when the cap came off could be determined within 0.02 s. In unsteady pressure measurements shielding the model is unnecessary since the data could be taken after the tunnel has reached stable conditions.

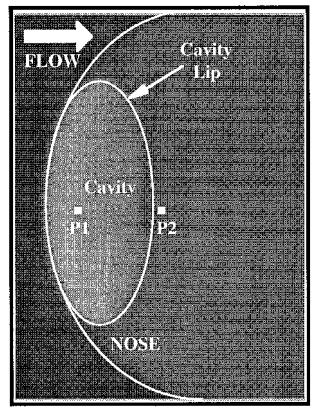

Fig. 2 Typical locations for temperature measurements on the thermal (IR) image.

In the PLMS technique, the freestream is seeded with a vapor (such as water or alcohol) in the stagnation chamber. This vapor then condenses because of the isentropic cooling it experiences as it expands through the supersonic nozzle, forming a fine condensate fog that provides an excellent medium for Mie scattering measurements. The light source was an Nd:YAG laser frequency doubled to 532 nm, and operated at 10 Hz. It provided about 70 mJ per pulse. The thin (250-μm) laser sheet formed by using a combination of cylindrical and spherical lenses was passed through the test section immediately upstream of the model nose. During the tunnel run, the scattering was imaged using a standard charge-coupled device video camera connected to a frame grabber installed in a personal computer. The laser and the frame grabber are synchronized for proper imaging. To make simultaneous fluctuating pressure measurements, the frame grabber sync signal is used both to start (trigger) the data acquisition in the LeCroy and to time the measurements by recording the frame grabber sync pulses on a separate LeCroy channel.

Analysis Procedure

Real-time thermal images recorded on video tapes during the tunnel run were processed by an IBM compatible personal computer system equipped with a Thermoteknix Therma-GRAM card and a color graphics card along with a video monitor. The computer system converts the analog video signal to a digitized (pixel) form; the temperature at each point (pixel) is then determined according to the brightness or the color of each pixel by using the temperature range information encoded in the video signal. Either still images at desired instants and/or surface temperature histories at desired points on the thermal image can be obtained.

To obtain the temperature history from thermal images, data can be read from video feed at 1/60-s intervals at the fastest rate. The temperature history at up to three selected regions on the model surface can be displayed on the computer screen or recorded in a data file. For a measurement area larger than a pixel, the computed temperature is the average over all pixels inside that area. In this study three regions of 3×3 pixels each were selected. An example is shown in Fig. 2 on a sample IR image for a large diameter/very deep cavity configuration. The data were further averaged in groups of 10 readings (spanning 0.17 s) to reduce detector noise and improve stability. Values at points at which the viewing angle plays a role were corrected using the angle sensitivity curve obtained during calibration.

Results

IR Images, General Characteristics

Figure 3 shows sample IR images for the bigger model (D_n = 5.08 cm) for various values of L/D (0.235–2.0) along with

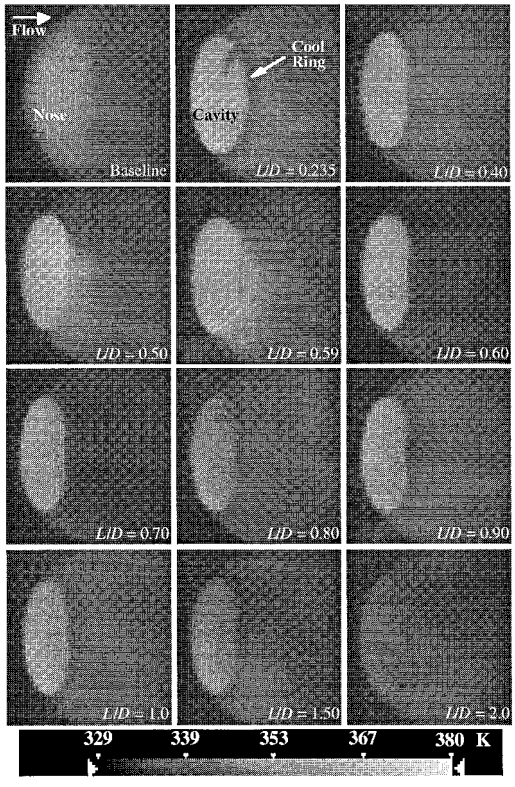

Fig. 3 Sample IR images for various cavities (all cases have sharp lip/flat base configuration obtained with bigger model).

the baseline case. These images are taken approximately 15 s after exposure to the freestream. Brighter regions represent higher temperatures as shown in the scale at the bottom of the figure. Several observations can be made:

1) For L/D = 0.235 and 0.40, the cool ring is present, although it appears weaker for the 0.40 case, which might be because of its being closer to the medium depth range where it disappears. Surface flow visualization experiments[10,11] show that the physical cause of the cool ring is the flow separation occurring at the sharp lip of the cavity. This separation is also seen in the numerical simulations of Engblom et al.[13] of Mach 5 flow over the same cavity geometry; the computed size of the separation region is in good agreement with the size of the cool ring on the IR images.

2) For L/D = 0.50, 0.59, 0.60, and 0.70, the cool ring cannot be observed. When the upper and lower portions of the images are compared it can be seen that the temperature field is nonaxisymmetric. This lack of symmetry makes comparisons with axisymmetric cases difficult, and one must be careful in interpreting the results. The cases L/D = 0.60 and 0.70 have much lower surface temperatures indicated by the darker regions over almost the entire external surface, whereas L/D = 0.50 and 0.59 cases have higher temperatures (brighter regions) outside of the cavity. The flow also appears to be very sensitive to small changes in the cavity depth as is evident from the two different temperature fields of L/D = 0.59 and 0.60 cases. Although it cannot be seen in these still images, real-time playbacks of the IR video of these cases show unstable and oscillatory temperature fields in and around the cavity. In this context, unstable implies a flow switching randomly and rapidly between distinct states rather than oscillating at constant frequency within a narrow range of amplitudes. This will be described in greater detail later.

3) For L/D = 0.80, 0.90, 1.0, and 1.50, the cool ring is observed again and has approximately the same size as the shallow cases. Although the temperature field and the cool ring appear to be quite axisymmetric from the still images, real-time videos exhibit an oscillatory behavior in which there are times when the external surface of the nose in the vicinity of the cavity becomes hotter (brighter) and at the same time cavity side-wall (internal surface) becomes colder (darker) for a short period. However, amplitudes are much lower compared to the previously mentioned unstable cavity cases. This will be evident in the temperature histories. The L/D = 1.5 case appears to be a highly promising one in that the overall temperature field is lower, and there is a cool ring that helps reduce temperatures even more.

4) The L/D = 2.0 case has a very low temperature field (darker areas) and looks the most promising for applications. Its real-time temperature image reveals a relatively weak oscillatory behavior. By maintaining a quite low mean temperature with small temperature fluctuations, this case is highly stable compared to the medium depth or other very deep cavity cases. However, fluctuating pressure measurements show very high-amplitude pressure oscillations on the base of the cavity, as will be discussed later. Another interesting feature is that the cool ring, which is clearly observable up to L/D = 1.5, is not observed for L/D = 2.0.

Temperature Histories

To compare different cases, attention is focused on a single point on the nose for all cases. This point ($P2$) is at about 33 deg from the model axis in all cases and stays within the cool ring for cases in which the cool ring is observed (see Fig. 2). Figure 4 shows the normalized temperature histories at $P2$. T is the model surface temperature, T_o is the tunnel stagnation temperature (in K), and T_i is the initial temperature at the measurement point. Most of the cases show temperature reduction relative to the baseline model. There are essentially two classes of temperature histories, one that is slightly lower and one that is much lower than the baseline level. The IR images show that in shallow and some of the very deep cavity cases, this is caused by the cool ring. Some deep cavity cases, L/D = 0.60 and 0.70 (not shown, but very similar to L/D = 0.60), in which no cool ring is observed, also show substantial reduction in surface temperatures that are quite unsteady as can be seen from Fig. 4. In fact, most cases exhibit highly oscillatory behavior except L/D = 0.235 and very deep ones L/D = 1.5 and 2.0. The most oscillatory temperature histories are those of L/D = 0.59 and 0.60. Although the 0.59 case has a high average (on the order of baseline levels), the 0.60 case has much lower values, and hence, a low average. This again brings out both the unstable nature and the extreme sensitivity to small changes in depth in this range. For much deeper cavity cases (L/D = 1.5 and 2.0), the temperature histories are much lower compared to the baseline case, and their temperature

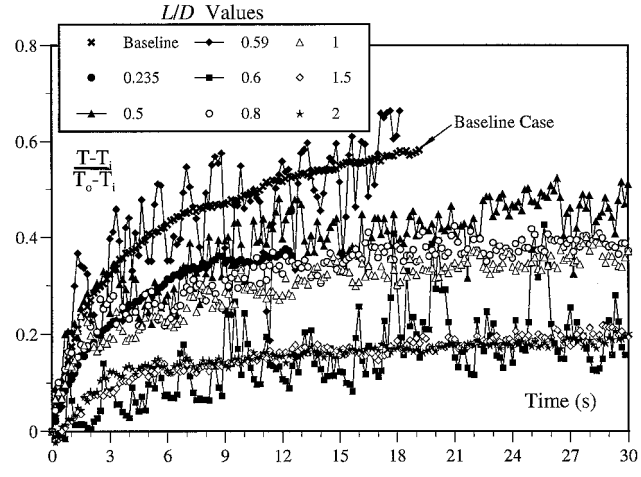

Fig. 4 Temperature histories at a point ($P2$) in the vicinity of the cavity lip for a sharp lip/flat base configuration with various L/D values.

histories are relatively stable. They are very promising cases for applications.

Heat Flux Histories

In this section, heat flux histories derived from the surface temperature histories using the semi-infinite solid assumption are presented for some representative cases. The method is discussed in detail in Ref. 14. The validity of the results is assessed by comparisons with the theoretical solution of Fay and Riddell[15] for stagnation point heating.

Figures 5a and 5b show the heat flux and the Stanton number histories, respectively, for the baseline case. The Stanton number is calculated from the heat flux as follows:

$$C_h = \frac{q}{\rho_\infty u_\infty c_p (T_{aw} - T_w)}$$

Except over the first few seconds, the measured heat flux and Stanton number histories at $P1$ (stagnation region) are about 20% below the Fay and Riddell values.[15] This discrepancy may be partly because of uncertainties in the temperature correction because of the viewing angle, the fact that locating the stagnation point precisely on the IR images is difficult and the assumption of a semi-infinite solid. It should also be noted that very high heat transfer rates that are calculated within the first second are because of the rapidly increasing nose temperature during the first few time-steps of data recording.

For a spherical nose, the surface heat flux varies as $\cos^{1.5}(\theta)$. Thus, the heat flux at $P2$ (at $\theta \approx 30$ deg) can also be estimated by using the values at $P1$ as well as calculated from the measured temperature history at $P2$. In Fig. 5a, it can be seen that the quantity $qP1 \times \cos^{1.5}(30\ \text{deg})$ is very close to the measured values at $P2$. This demonstration confirms the relative accuracy of the temperature measurements. The corresponding Stanton numbers are shown in Fig. 5b. Note that the Fay and Riddell values[15] in this case reduce to a constant because of the normalization process. For a cavity case, the semi-infinite solid assumption is questionable at $P2$ because of small wall thickness at this point.

Figure 6 shows the normalized heat flux (q/q_b, where q_b is the baseline-stagnation region heat flux) histories at $P2$ for progressively increasing cavity depths along with the baseline case for comparison. All of the data sets have $q/q_b < 1$, and thus, all have lower average heat flux than the baseline stagnation levels. Cases with $L/D = 0.50$–1.0 have oscillatory heat flux histories, which are consistent with their oscillatory temperature histories. Large variations are observed for the 0.50 and 0.60 cases, with values of q/q_b as low as 30–40% of the baseline stagnation region values as well as up to 20% above the baseline values. The highly unstable temperature history of the case $L/D = 0.60$ (see Fig. 4), is responsible for the high peaks and troughs observed in the heat flux history. The case $L/D = 1.5$ has values of q/q_b at $P2$ almost equal to those for $L/D = 2.0$. This is simply because the $L/D = 2.0$ case, although it has very low temperatures, does not have the cool ring, which is present in the $L/D = 1.50$ case. The cool ring probably causes the q/q_b values for the $L/D = 1.50$ case to be on the order of those for the $L/D = 2.0$ case.

There appear to be at least two mechanisms that can result in reduced heating rates. First, the nose-cavity can reduce the mean velocity gradient over the nose (hence, reducing heating). Second, computations[16] show that for deep cavities the shock velocity can be quite high (up to 20% of the free-stream velocity). As the shock moves downstream the relative Mach number drops and the temperature rise across it decreases. When it moves upstream the opposite occurs; however, this occurs during the period of outflow of air from the cavity which is relatively cool. This cool outflow essentially shields the body surface.

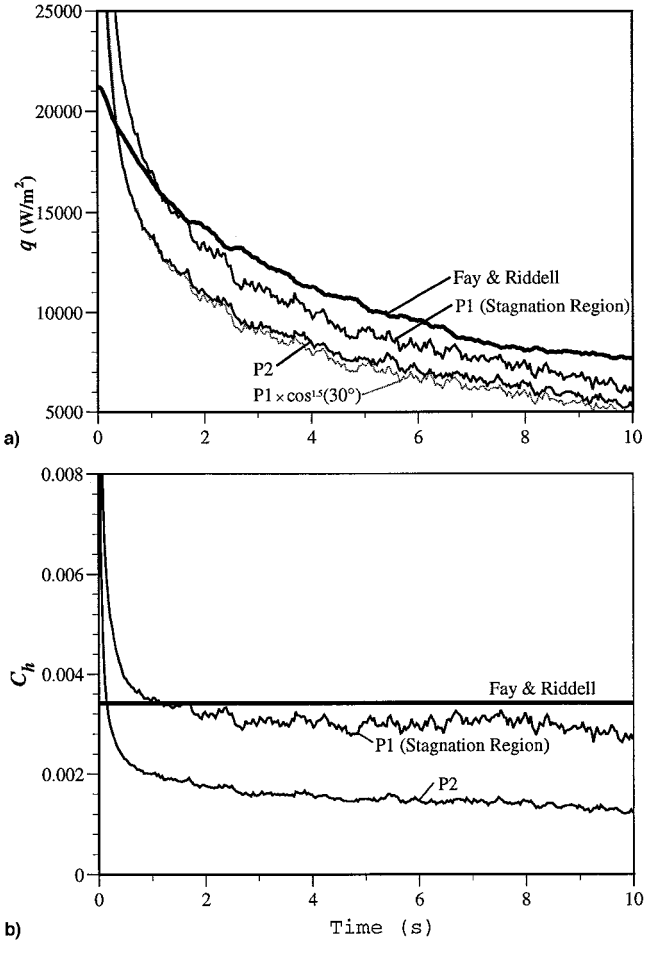

Fig. 5 Comparison of heat transfer in baseline case with Fay and Riddell theory[15]: a) heat flux and b) Stanton numbers.

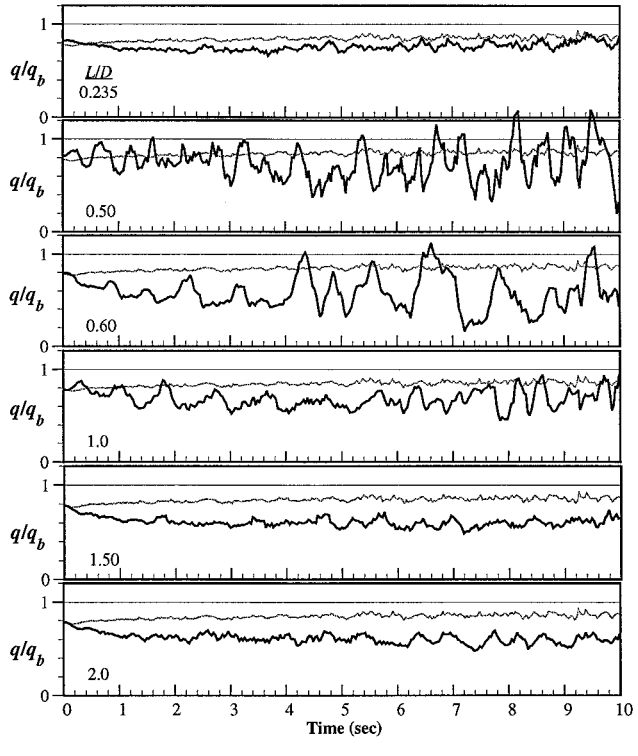

Fig. 6 Heat transfer rates at $P2$ normalized by the baseline (stagnation region) values q_b for various cavity sizes. Thin dotted-curve: heat transfer rates at $P2$ for the baseline case.

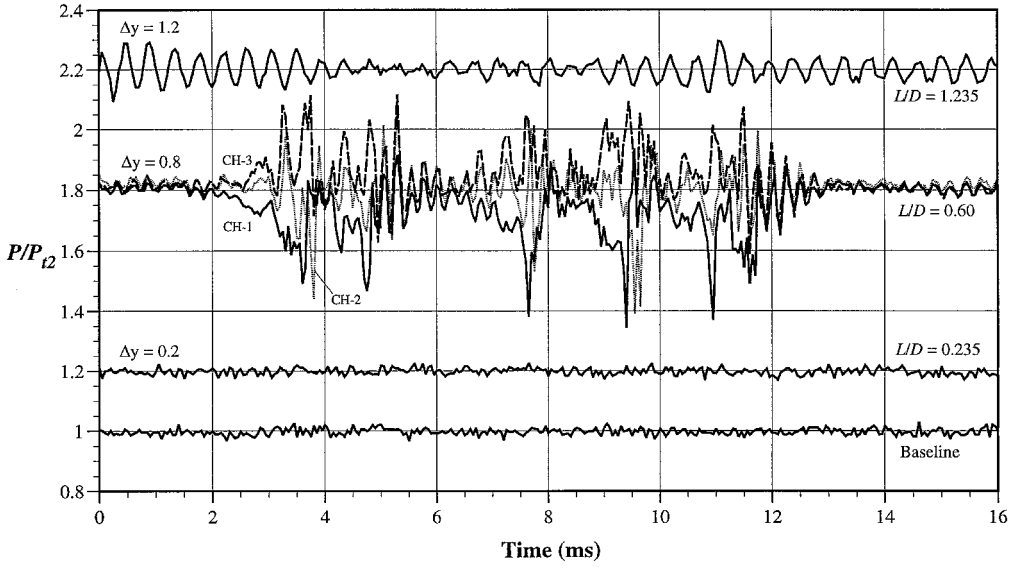

Fig. 7 Sample pressure signals for different cavity depths (Δy are vertical offset values of the plots in each case).

Fluctuating Pressures, General Characteristics

Figure 7 shows portions of the pressure signals measured at the cavity base, and Fig. 8 shows the corresponding normalized power spectra for various cavity depths. Data in these figures were obtained using the bigger (D_n = 5.08 cm) model. Cases other than the baseline in Fig. 7 are offset vertically by increments in P/P_{t2} denoted by Δy. Shallow cavity (L/D = 0.235) pressure signals are qualitatively similar to the baseline case with small rms values (1.15% of the freestream pitot pressure P_{t2}), although their power spectra reveal certain resonance frequencies, unlike the baseline spectrum, which is broadband (see Fig. 8). Further, for the shallow range, all data records are similar, indicative of one mode of oscillation. In contrast, the medium depth cavity (L/D = 0.60) pressure signals are characterized by random switching between two modes that have different amplitudes but similar frequencies (the power spectrum of this case in Fig. 8 indicates a strong peak at about 4 kHz). The power spectrum also indicates some energy concentration at frequencies below 1 kHz, which might be characteristic of the switching frequency of this unstable behavior. However, the record length (1024 data points) is too small to resolve such low-frequency phenomena accurately.

Further examination of the medium depth case shows that the signals from all three locations (channels 1, 2, and 3) on the base often have similar behavior, although it is worth noting certain characteristics of the transition to high-amplitude oscillations. The high-amplitude mode starts with decreasing pressure levels on channel 1 and increasing levels on channel 3 (e.g., around 3 ms). Pressure levels on channel 2 are usually between those on channels 1 and 3. This imbalance of the pressure field is either a triggering mechanism for high-amplitude oscillations, or is a result of a nonaxial oscillation mode perhaps involving radial or slosh modes. Before returning to the low-amplitude mode all three channels experience similar (almost all at the same phase) oscillations, suggesting that the pressure wave inside the cavity becomes one-dimensional toward the end of the high-amplitude mode. Such behavior occurs at random intervals and for random time spans throughout the entire data string. This makes the results of standard statistical analysis difficult to interpret since the overall rms does not truly reflect either condition. The lack of flow symmetry and the irregular high-temperature spots observed around the lip in the medium depth cavity cases are probably caused by switching between different oscillation modes. This type of oscillation is observed in other medium depth cavity cases ($0.40 \leq L/D \leq 0.70$) with various lip and base shapes and for both the smaller and bigger models.

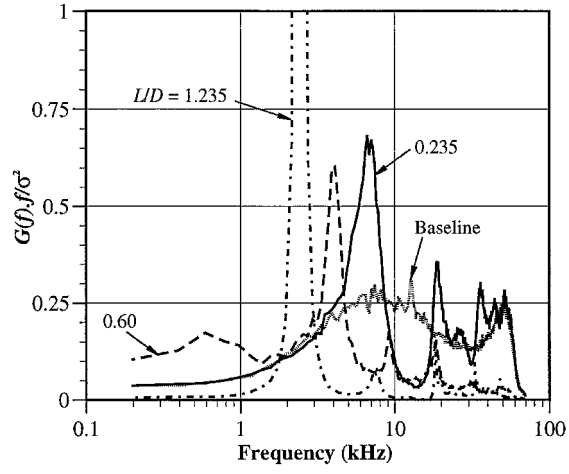

Fig. 8 Normalized power spectra of the pressure signals shown in Fig. 7.

Figure 7 also shows pressure signals for L/D = 1.235 in which the oscillations are nearly sinusoidal with varying amplitudes. Measurements made with the smaller model show that for higher values of L/D, signals become even more sinusoidal with almost constant amplitude (at a fixed L/D). Amplitudes tend to increase with increasing L/D. The extremely sharp peak in the power spectrum around 2 kHz for L/D = 1.235 (Fig. 8), confirms the highly oscillatory nature of this case. Since the vertical axis is the normalized power this plot only brings out the dominant frequencies and harmonics. The power spectra in absolute units show the relative power levels of the fluctuations for different cases. The high-amplitude oscillations in the L/D = 0.60 case have much higher power content at almost all frequencies compared to the other cavity cases. The sole exception is the L/D = 1.235 case at its primary resonance frequency.

Figure 9 shows the variation of the normalized standard deviation of the pressure oscillations with L/D. D is varied only for the bigger model [D_n = 5.08 cm (2.0 in.)], and is fixed at $1/2D_n$ for the smaller model [D_n = 3.05 cm (1.2 in.)]. Note that three data sets are labeled HM, for high-amplitude mode. The standard deviation of the HM is calculated by using only the high-amplitude portions of the pressure signal. Details of the calculation procedure are given in Ref. 14. The results show that the bimodal oscillation is observed only within approximately $0.35 \leq L/D \leq 0.70$. In most of the other deeper

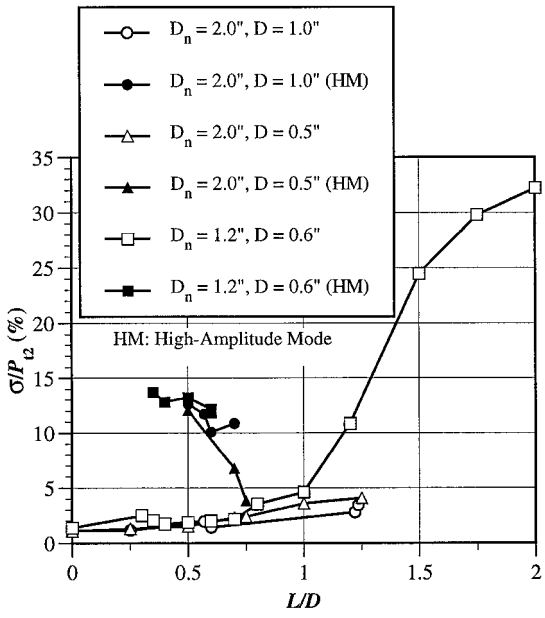

Fig. 9 Variation of standard deviation of pressure signals with *L/D*.

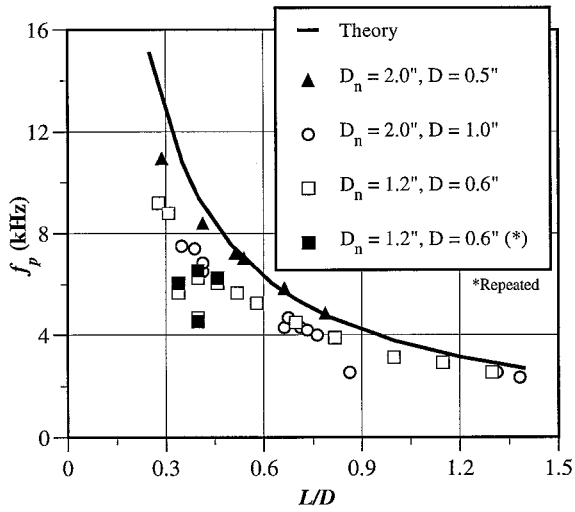

Fig. 10 Primary resonance frequencies measured in the cavity.

cavity cases, even though the oscillations have a highly sinusoidal character, they have a varying envelope. However, there is no sudden change in amplitude as observed in bimodal cases and the variation in amplitudes is smaller. Beyond the bimodal range, the overall standard deviation of the fluctuations increases smoothly with the cavity depth attaining very large values at $L/D = 2$. However, the rate of increase decreases as L/D increases further. Cavities with small diameter [$D = 1.27$ cm (0.5 in.)] also exhibit bimodal behavior (Fig. 9).

All of the cavity configurations exhibit oscillatory flow because of resonance. The lowest distinctive frequency is considered the primary resonance frequency and can be calculated from simple linear theory given the cavity depth and the speed of sound inside the cavity. In the classic organ pipe mode the wavelength λ_p of the primary resonance is given as $\lambda_p = 4L$. Thus, the frequency f_p corresponding to this wavelength can be obtained knowing the speed of sound a. Assuming that the gas temperature inside the cavity is approximately the stagnation temperature T_0 of the flow, f_p becomes $f_p = a/\lambda_p$, where $a = \sqrt{\gamma RT_0}$. Combining these relations

$$f_p = \sqrt{\gamma RT_0/4L}$$

Since the pressure waves travel between the shock wave and the cavity base, a more appropriate value of L is the distance, from the mean location of the bow shock to the cavity base L', rather than from the lip to the cavity base. For the baseline case δ can be estimated using correlations.[17] For a spherical nose

$$\delta/R_n = 0.143 \exp(3.24/M_\infty^2)$$

Hence, at $M_\infty = 4.95$, δ is about $0.08D_n$. And as a first-order approximation of L', this distance has been added to all physical cavity depths L.

Figure 10 shows the measured and predicted frequencies. Experimental frequencies are obtained from the power spectra. Since cavity diameter is not considered in calculating theoretical values, the agreement with the measurements is poorer for shallower cavities. However, the experimental trend for f_p vs L/D is the same as the theory and excellent agreement between experiment and theory is obtained for much deeper cavity cases.

The bimodal behavior observed in the medium depth cavities is specific to this particular range and is not observed in any other cavity depth range. As noted earlier, numerical[12,13] studies made with clean freestream conditions do not generate such instabilities over the medium depth cavity range and suggest that this phenomenon could be triggered by freestream disturbances that are present in the wind-tunnel flow. However, the fact remains that the cavities within this particular L/D range exhibit very strong amplifications of these disturbances that are present in all other cavity cases but are not amplified nearly as much (i.e., $L/D = 1.235$ case). The shock-wave shapes obtained in this case are similar to those observed by Huebner and Utreja[8] at Mach 10 for a somewhat different nose-cavity model but at a similar cavity depth ($L/D \sim 0.60$). Stallings and Burbank[3] also report unsteady (unpredictable, sporadic) flow for their concave-nose cylinder model that had an L/D of 0.5, where L is the radius of the concave cavity surface. Also, the schlieren photographs of the bow shock wave in Ref. 3 were similar to the shapes seen in both Ref. 8 and the present study. If this unstable behavior is triggered by wind-tunnel disturbances, it is not unique to the present facility. It has been observed in other facilities and with different nose-cavity models.

Instantaneous Shock Shapes and Corresponding Pressure Histories

Some examples of instantaneous shock shapes obtained with the PLMS technique along with base pressure histories around the time when the shock shape was recorded are presented in this section. The results were obtained using the larger ($D_n = 5.08$ cm) model.

Figure 11 shows examples for the flat-faced baseline ($L/D = 0$) and a shallow cavity ($L/D = 0.23$) case. The vertical line at zero in the time scale of the pressure history is the time when the image was taken. The images are annotated such that the location of the pressure transducer (denoted by CH-2) on the cavity base (in the baseline case, the nose face) and the relative cavity size can be seen. The black region upstream of the model corresponds to the region downstream of the shock, therefore the shock itself is indicated by the boundary of the black and gray regions. The flat surface of the model nose is between the two parallel black lines shown in the figure, which are drawn to indicate the cavity insert. In this image (and all others for this case), the shock is symmetric and the standoff distance is constant. The low-amplitude pressure signals shown are the freestream pitot pressure fluctuations in the wind tunnel since there is no cavity to generate resonance. This result shows that under the influence of freestream fluctuations, a very stable and axisymmetric bow shock is present in front of the model.

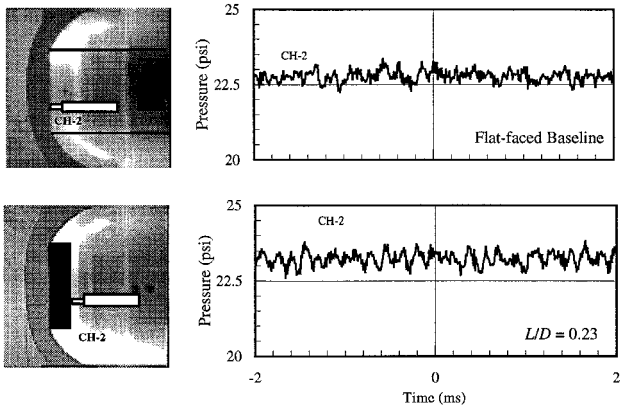

Fig. 11 Instantaneous shock-wave shapes and corresponding pressure histories for the flat-faced baseline (L/D = 0) and the shallow cavity (L/D = 0.23) cases.

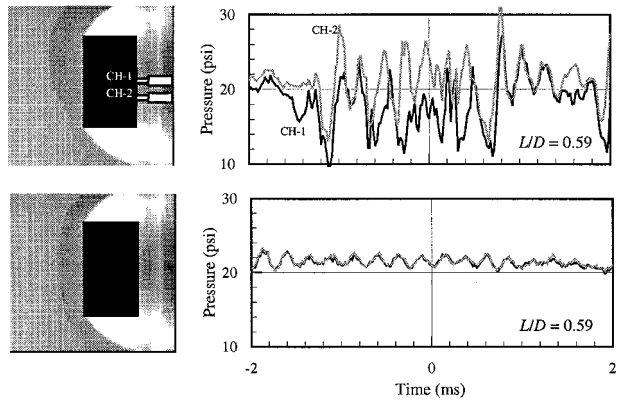

Fig. 12 Instantaneous shock-wave shapes and corresponding pressure histories for the medium depth cavity case (L/D = 0.59).

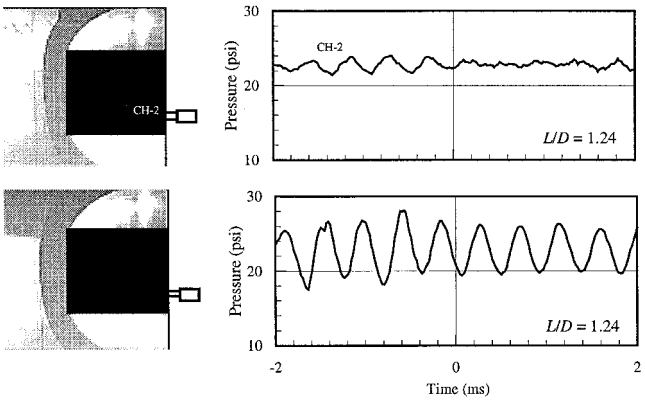

Fig. 13 Instantaneous shock-wave shapes and corresponding pressure histories for the very deep cavity case (L/D = 1.24).

In the L/D = 0.23 case (bottom part of Fig. 11), shock shape is still axisymmetric, and the position of the shock is invariant (in almost all of the 68 frames, there is no indication of shock-wave motion). The amplitude of the base pressure signal, on the other hand, has increased slightly because of the presence of the cavity, but has little impact on either the shock shape or its position.

As the cavity depth is increased into the unstable bimodal range, shock shapes begin to change because of the strong oscillations. Two examples of shock shapes for L/D = 0.59 are shown in Fig. 12. Note that the pressure scale is much larger in this case than in the previous figure. When the pressure signal is in the low-amplitude mode (bottom plot), the shock shape is symmetric and the standoff distance is close to that of baseline levels. In contrast, when the pressure is in the high-amplitude mode (top plot) the shock has a bulge toward the upper portion and the local shock standoff distance is almost twice that of the baseline case. This clearly brings out the nonsymmetrical nature of the medium depth cavity cases as observed in other results. Note that when the shock shape is irregular, both channels have different pressure levels at a given time, whereas they have regular (simultaneous) oscillations when the shock appears to be symmetric and at the expected distance upstream of the model. This behavior is generally observed in most of the 132 shock shapes recorded. In a few cases, the bulge in the upper portion is observed in the lower part of the shock (5% of all the images).

Finally, two examples for the L/D = 1.24 (very deep) case are shown in Fig. 13. In this case, only one channel (channel 2) of pressure data was taken. Earlier results showed that all channels exhibit similar and simultaneous oscillations. In this cavity range the shock shapes regain their symmetric characteristics, but it appears that the standoff distance is now somewhat affected by the strong oscillations. The bottom image has a standoff distance that is slightly larger than the other, whereas the pressure history shows relatively larger-amplitude oscillations. Similar results are observed in the other 32 images for this case. In all of the images, shocks are symmetric and the variation in the standoff distance is small.

In summary, instantaneous shock shapes are consistent with the behavior of the pressure and temperature measurements. Bimodal pressure oscillations and irregular temperature distributions observed in the medium depth cavity cases correspond to large variations in shock shape. Regular and symmetrical shock shapes obtained in other cavity cases show the uniqueness of this behavior to this particular L/D (medium-depth) range. The fact that the shock shapes return to normal for the very deep cavity case suggests that the promising cases in this range (L/D = 1.50 and 2.0) may also have regular shock structure that may provide better stability and control during flight.

Conclusions

The results show the following facts for a hemisphere–cylinder model with an axial nose-cavity:

1) The external surface temperature history is a strong function of cavity depth (L/D). Other than the case L/D = 0.59, which has a highly oscillatory temperature history with levels comparable to the baseline case (i.e., no cavity), the temperatures are lower than the baseline case in all cases. In terms of practical applications, the case L/D = 2.0 looks particularly promising, since it has a relatively stable and much-reduced temperature history compared to the baseline case. Within the range $0.4 \leq L/D \leq 0.7$, the external temperature field and the resulting temperature histories exhibit random changes and oscillatory behavior, which is believed to be tied to the particular pressure oscillations within this range.

2) Resonance because of the presence of the cavity becomes stronger as L/D increases; the oscillation frequency agrees well with predictions of organ pipe theory in almost all cases. Within the range $0.4 \leq L/D \leq 0.7$, the pressure signals are characterized by random switching between two modes that have different amplitudes but similar frequencies, and which are nonaxisymmetric. Similar effects are seen in the temperature histories. For $L/D \geq 1$, the base pressure amplitudes become very large (up to 30% of the freestream pitot pressure) and may be of concern from an aerodynamics/stability viewpoint. Further study is needed to investigate this aspect of the problem.

3) Instantaneous shock-shape images confirm the nonaxisymmetric behavior of certain cases and correlate with bimodal pressure oscillations. In the cases where only single-mode, large-amplitude pressure oscillations are observed, the shock undergoes upstream and downstream motion, but appears quite symmetrical.

Acknowledgments

Support for the project was provided in part by the Institute for Advanced Technology, University of Texas at Austin under the U.S. Army Armaments Research, Development, Engineering Center Contract DAAA21-93-C-0101. The authors are grateful to the Center for Energy Studies of the University of Texas at Austin for the loan of the infrared camera system. The authors are also grateful to Noel Clemens and the graduate students of the Flowfield Imaging Laboratory at the University of Texas at Austin for development of the planar laser scattering system in the Mach 5 wind tunnel. The suggestions of Dennis Wilson are also gratefully acknowledged.

References

[1]Hohler, V., and Stilp, A. J., "Long Rod Penetration Mechanics," *High Velocity Impact Mechanics*, edited by Jonas A. Zukas, Wiley, New York, 1990, Chap. 5.

[2]Baker, J., and Williams, A., "Hypervelocity Penetration of Plate Targets by Rod-Like Projectiles," *International Journal of Impact Engineering*, Vol. 5, 1987, pp. 101–110.

[3]Stallings, R. L., and Burbank, P. B., "Heat-Transfer and Pressure Measurements on a Concave-Nose Cylinder for a Mach Number Range of 2.49 to 4.44," NASA TMX-221, Oct. 1959.

[4]Huebner, L. D., and Utreja, L. R., "Experimental Flowfield Measurements of a Nose Cavity Configuration," Society of Automotive Engineers, Paper 871880, Warrendale, PA, Oct. 1987.

[5]Sambamurthi, J. K., Huebner, L. D., and Utreja, L. R., "Hypersonic Flow over a Cone with Nose Cavity," AIAA Paper 87-1193, June 1987.

[6]Marquart, E. J., Grubb, J. B., and Utreja, L. R., "Bow Shock Dynamics of a Forward-Facing Nose Cavity," AIAA Paper 87-2709, Oct. 1987.

[7]Utreja, L. R., and Gurley, W. H., "Aircraft Hollow Nose Cone," U.S. Patent 4,850,275, BDM International, Huntsville, AL, July 1989.

[8]Huebner, L. D., and Utreja, L. R., "Mach 10 Bow-Shock Behavior of a Forward-Facing Nose Cavity," *Journal of Spacecraft and Rockets*, Vol. 30, No. 3, 1993, pp. 291–297.

[9]Yuceil, B., Dolling, D. S., and Wilson, D., "A Preliminary Investigation of the Helmholtz Resonator Concept for Heat Flux Reduction," AIAA Paper 93-2742, July 1993.

[10]Yuceil, B., and Dolling, D. S., "Effects of a Nose Cavity on Heat Transfer and Flowfield over a Blunt Body at Mach 5," AIAA Paper 94-2050, June 1994.

[11]Yüceil, B., and Dolling, D. S., "Nose Cavity Effects on Blunt Body Pressure and Temperatures at Mach 5," *Journal of Thermophysics and Heat Transfer*, Vol. 9, No. 4, 1995, pp. 612–619.

[12]Engblom, W. A., Goldstein, D. B., Ladoon, D., and Schneider, S. P., "Fluid Dynamics of Hypersonic Forward-Facing Cavity Flow," AIAA Paper 96-0667, Jan. 1996.

[13]Engblom, W. A., Yuceil, B., Goldstein, D. B., and Dolling, D. S., "Hypersonic Forward Facing Cavity Flow: An Experimental and Numerical Study," AIAA Paper 95-0293, Jan. 1995.

[14]Yüceil, K. B., "An Experimental Investigation of a Forward-Facing Nose Cavity on a Blunt Body at Mach 5," Ph.D. Dissertation, Dept. of Aerospace Engineering and Engineering Mechanics, Univ. of Texas, Austin, TX, Dec. 1995.

[15]Fay, J. A., and Riddell, F. R., "Theory of Stagnation Point Heat Transfer in Dissociated Air," *Journal of the Aeronautical Sciences*, Vol. 25, No. 2, 1958, pp. 73–85.

[16]Engblom, W. A., "Numerical Investigation of Hypersonic Flow over a Forward-Facing Cavity," Ph.D. Dissertation, Dept. of Aerospace Engineering and Engineering Mechanics, Univ. of Texas, Austin, TX, Aug. 1996.

[17]Anderson, J. D., "Correlations for Hypersonic Shock-Wave Shapes," *Hypersonic and High Temperature Gas Dynamics*, McGraw–Hill, New York, 1989, pp. 189–192.